

The Bean-Livingston barrier in mesoscopic type I and type II superconductors

Alexander D. Hernández^{1,2} and Daniel Domínguez²

¹*Laboratorio de Superconductividad, Facultad de Física-IMRE, Universidad de la Habana, 10400, Ciudad Habana, Cuba.*

²*Centro Atómico Bariloche, 8400 San Carlos de Bariloche, Río Negro, Argentina*

We study the influence of the Bean-Livingston barrier on the field penetration in mesoscopic samples of both type I and type II superconductors. Our results are obtained from numerical simulations of the time-dependent Ginzburg-Landau equations considering two different boundary conditions. For the superconductor-insulator boundary condition (S-I) we study the dependence of the first field for flux penetration (H_p) with the Ginzburg-Landau parameter (κ) observing an increase of H_p with decreasing κ . However, the superconductor-normal boundary condition (S-N) shows a different behavior: H_p is independent of κ and equal to H_c . In particular this implies that the S-N boundary condition completely suppresses the Bean-Livingston barrier for type I superconductors. We also study the magnetization curves at different samples dimensions. In the region where the transition from a macroscopic to a mesoscopic behavior takes place, we show that vortices located inside the sample induce a reinforcement of the surface barrier at fields greater than the first penetration field. We study the sample size dependence of the first, second and third penetration fields.

PACS numbers: 74.20.De, 74.25.Ha, 74.60.Ec

I. INTRODUCTION

In the last years there has been an important experimental and theoretical interest in the study of vortex physics in a mesoscopic scale.¹⁻³ The statistical properties of these systems are not well explained with the usual statistics of a large number of strongly interacting vortices and a detailed knowledge of the interaction between the vortex and the sample surface is needed.

The interaction between vortices and the surface currents manifests itself fundamentally in the existence of the Bean-Livingston barrier⁴ which delays the vortex penetration and generates metastable states. Without the surface effects the penetration of magnetic field becomes energetically favorable at the first critical field H_{c1} , however the energy barrier prevents the entry until a higher field H_p at which the barrier no longer exists. H_p , also known as the superheating field, is associated with the peak in the magnetization curves and is strongly influenced by the presence of surface irregularities.

The study of the Bean-Livingston (B-L) barrier has attracted a renewed interest recently in the study of mesoscopic superconductors. For example, Enomoto and Okada⁵ by means of numerical simulations of the time-dependent Ginzburg-Landau equations (TDGL), studied the influence of temperature and surface irregularities on the surface barrier. Sonin and Traito⁶ showed that the presence of the B-L barrier affects the entry and exit of vortices influencing the surface resistance. They found a surface-induced suppression of the ac losses.

Another important line of research of mesoscopic superconductors are the Al disks.^{1,3,7-13} Recent advances in the microfabrication technology and measurement techniques now allow the fabrication and study of superconducting particles with sizes comparable to the coherence length (ξ). Most of the studies were done in Al disks, $\kappa \simeq 0.3$ a type I material, however for small samples the

effective penetration depth $\Lambda = \lambda^2/d$ increases for decreasing disk thickness (d) resulting in effective κ values in the type II region that can be studied theoretically using the Ginzburg-Landau equations. In this regime the Al disk can develop Abrikosov multivortex states⁸ and depending on the radius (R) and thickness of the disk it is possible to observe first or second order phase transitions,⁷ by increasing the disk sizes the second order reversible phase transition observed for small disk radius is replaced by a first order transition. There is also an intermediate regime where jumps in the magnetization appear associated with the vortex entrance.

Other interesting phenomena have been studied for mesoscopic Al disk, for example in Ref. 13 the hysteresis in the magnetization curves were observed experimentally and explained in terms of the presence of the Bean-Livingston barrier and in Ref. 11 the behavior of the third critical field H_{c3} was investigated for different sample sizes and geometries.

On the other hand, only few theoretical studies on the TDGL equations have been done in superconductors with type I behavior, possibly because the theory is better to describe a superconductor near a second order phase transition at a temperature near T_c . In this framework Gorkov and Eliasberg¹⁴ proved an equivalence between the microscopic BCS theory and the TDGL equations. Moreover, experimental results frequently show that the TDGL predictions are often valid in a higher range of temperature and magnetic fields. In this regime, i.e. high temperatures and magnetic fields, the TDGL equations can also be valid in the type I region. In this paper, we present numerical simulation of the complex TDGL equations to study the Bean-Livingston barrier in mesoscopic samples.

In the first part of the paper we study the dependence of H_p with the Ginzburg-Landau parameter κ ($\kappa = \lambda/\xi$), exploring both the type I ($\kappa < (1/\sqrt{2})$) and the type

II region ($\kappa > (1/\sqrt{2})$). We study the effects of the B-L barrier from a comparison of two types of boundary conditions. (i) The superconductor-insulator (S-I) boundary condition: consisting in the vanishing of the superconducting current perpendicular to the boundary ($\mathbf{J}_s \cdot \hat{\mathbf{n}} = 0$). In this case we find an increase of H_p with decreasing κ . (ii) The superconductor-normal (S-N) boundary condition: approximated as the vanishing of the superconducting order parameter at the boundary ($\Psi = 0$). A different behavior is observed for the S-N boundary condition, the field H_p is independent of κ and equal to H_c . In particular, this result shows that in the type I region the boundary condition $\Psi = 0$ suppresses completely the Bean-Livingston barrier. The S-N boundary condition also inhibits the nucleation of the surface superconductivity as we observe in the magnetization curves.

In the second part of the paper we study magnetization curves in type II superconductors at different sample dimensions in the region where the transition from a macroscopic to a mesoscopic behavior takes place. We study the change of vortex configurations in the vicinity of the magnetization discontinuities that appear in mesoscopic samples. We show that these great discontinuities appear because in mesoscopic superconductors the vortices that are inside the sample induce a reinforcement of the surface barrier at fields greater than the first penetration field. In this way, it is possible to define a second, third, fourth, etc. penetration fields that are a consequence of the interaction between vortices and the surface currents. We study the samples size dependence of the first, second and third penetration fields for the S-N and S-I boundary conditions and we show that for sufficiently large sample sizes the known macroscopic behavior is recovered, i.e. a continuous magnetization curves appears since $H_{p3} \rightarrow H_{p2} \rightarrow H_p$. We also found that the magnetization discontinuities appear even in the region of surface superconductivity, emphasizing that also in the state of surface superconductivity the magnetic field penetrates the sample in quantized units.

II. MODEL AND DYNAMICS

Our numerical simulations are carried out using the time-dependent Ginzburg-Landau equations complemented with the appropriate Maxwell equations. In the zero-electric potential gauge we have:^{15,16}

$$\frac{\partial \Psi}{\partial t} = \frac{1}{\eta} [(\nabla - iA)^2 \Psi + (1 - T)(1 - |\Psi|^2)\Psi] \quad (1)$$

$$\frac{\partial A}{\partial t} = (1 - T) \text{Im}[\Psi^*(\nabla - iA)\Psi] - \kappa^2 \nabla \times \nabla \times A \quad (2)$$

where Ψ and A are the order parameter and vector potential respectively and T is the temperature. Equations (1) and (2) are in its dimensionless form. Lengths have been scaled in units of $\xi(0)$, times in units of

$t_0 = \pi\hbar/(96k_B T_c)$, A in units of $H_{c2}(0)\xi(0)$ and temperatures in units of T_c . η is proportional to the ratio of characteristic times for Ψ and A .

We have used the standard finite difference discretization scheme to solve equations (1) and (2).¹⁵ The order parameter and vector potentials are defined at the nodes of a rectangular mesh ($\vec{r} = (I, J)$), and the link variables $U_{\mu I, J} = \exp(-i\kappa h_\mu A_{\mu I, J})$ ($\mu = x, y$) are introduced in order to maintain the gauge invariance under discretization. The dynamical equations must be completed with the appropriate boundary conditions for both the order parameter and the vector potential. The order parameter has two relevant boundary conditions, which depend on the materials at the interface. One possible boundary condition is:

$$(\Pi\Psi)^\perp = (\nabla - i\vec{A})^\perp \Psi = 0 \quad (3)$$

usually known as the superconductor-insulator boundary condition (S-I) because it implies that the perpendicular component of the superconducting current is equal to zero at the surface ($\vec{J}_s^\perp = 0$). This is the most frequently used boundary condition because it also minimizes the free energy at the sample surface.

A very different boundary condition is

$$\Psi = 0, \quad (4)$$

which approximately describes a superconductor-normal metal interface (S-N), and also it is similar to having a high density of defects at the interface. This boundary condition completely suppresses the surface currents ($\vec{J}_s^\perp = \vec{J}_s^\parallel = 0$) and maximizes the surface Helmholtz free energy, which becomes equal to the free energy of a normal metal.

These two boundary conditions are particular cases of the general condition:¹⁷

$$(\nabla - i\vec{A})^\perp \Psi = \frac{\Psi}{b} \quad (5)$$

where b is a surface extrapolation length which embodies the surface enhancement or suppression of the superconducting order parameter. The S-I condition appears when $b \rightarrow \infty$ and the S-N condition represent the case of metal-superconductors interfaces with $b \rightarrow 0$ as for example a ferromagnet-superconductor surface¹⁸ (for a detailed discussion on boundary conditions in the framework of the Ginzburg-Landau equations see Ref. 17). In any case, we will study the Bean-Livingston barrier by means of a comparison between these two conceptually different boundary conditions of the order parameter.

The boundary conditions for the vector potentials $A_{\mu I, J}$ are obtained by making

$$B = \nabla \times A = H_a$$

at the sample surface (where H_a is the applied magnetic field). In our simulations we have assumed a sample that

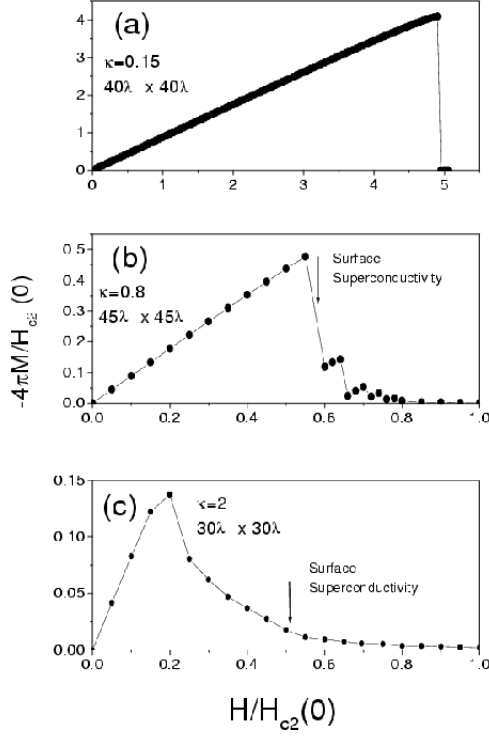


FIG. 1. Magnetization curves obtained using the S-I boundary condition: (a) $\kappa = 0.15$, (b) $\kappa = 0.8$ and (c) $\kappa = 2$. (Inserted in the figure are the size of the superconducting region used in the simulation, (ξ) is the coherence length).

has a square shape in the x, y direction and it is infinite in the z direction. We apply the magnetic field parallel to the z direction, the symmetry of the problem then implies for all mesh points $A_{I,J} = (A_{xI,J}, A_{yI,J}, 0)$ and $\mathbf{B}_{I,J} = (0, 0, B_{zI,J})$, where $B_{zI,J} = (\nabla \times \vec{A})_z = (\partial_x A_{yI,J} - \partial_y A_{xI,J})$.

In these geometries the discretized form of equations (1) and (2) are:

$$\begin{aligned} \frac{\partial \Psi}{\partial t} = & \frac{1}{\eta} \left(\frac{U_{xI,J} \Psi_{I+1,J} - 2\Psi_{I,J} + U_{xI-1,J} \Psi_{I-1,J}}{(\Delta x)^2} + \right. \\ & \left. + \frac{U_{yI,J} \Psi_{I,J+1} - 2\Psi_{I,J} + U_{yI,J-1} \Psi_{I,J-1}}{(\Delta y)^2} + \right. \\ & \left. + (1 - \frac{T}{T_c})(1 - |\Psi_{I,J}|^2) \Psi_{I,J} \right) \end{aligned} \quad (6)$$

$$\begin{aligned} \frac{\partial A_{xI,J}}{\partial t} = & (1 - \frac{T}{T_c}) \frac{\text{Im}[U_{xI,J} \Psi_{I,J}^* \Psi_{I+1,J}]}{\Delta x} - \\ & - \kappa^2 \left(\frac{B_{zI,J} - B_{zI,J-1}}{\Delta y} \right) \end{aligned} \quad (7)$$

$$\begin{aligned} \frac{\partial A_{yI,J}}{\partial t} = & (1 - \frac{T}{T_c}) \frac{\text{Im}[U_{yI,J} \Psi_{I,J}^* \Psi_{I,J+1}]}{\Delta y} - \\ & - \kappa^2 \left(-\frac{B_{zI,J} - B_{zI-1,J}}{\Delta x} \right) \end{aligned} \quad (8)$$

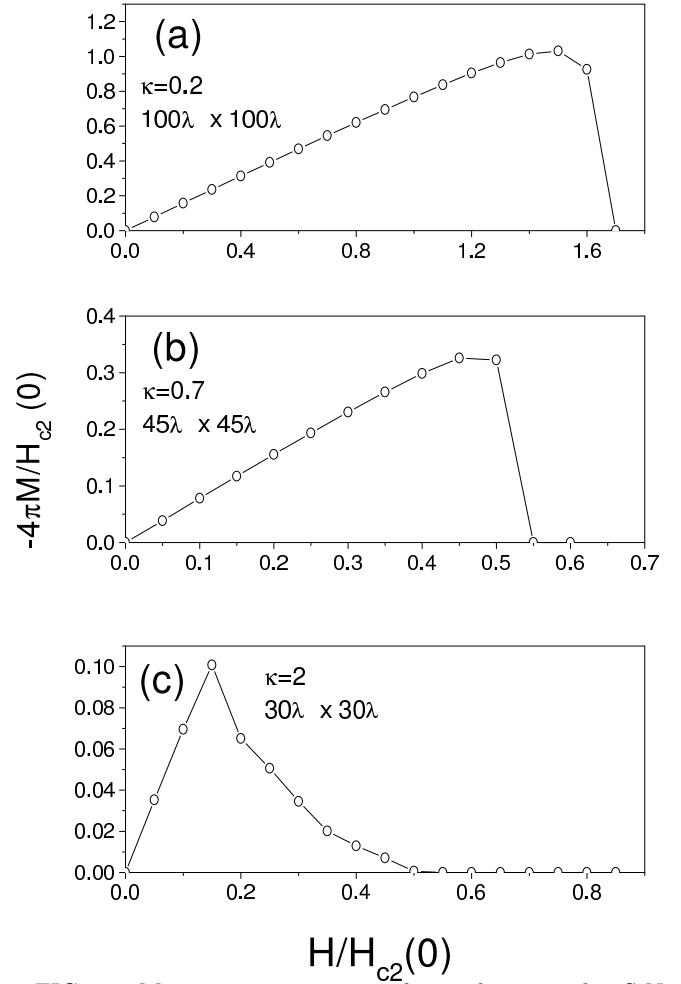


FIG. 2. Magnetization curves obtained using the S-N boundary condition: (a) $\kappa = 0.2$, (b) $\kappa = 0.7$ and (c) $\kappa = 1.8$.

where Δx and Δy are the mesh widths of the spatial discretization.

III. BEAN-LIVINGSTON BARRIER IN MACROSCOPIC SAMPLES

The magnetization curves for the S-I boundary condition are summarized in Fig.1 and for the S-N boundary condition are summarized in Fig.2. In both cases the curves were obtained initializing the variables to a perfect Meissner state [$\Psi(I, J, t=0) = 1$ and $A(I, J, t=0) = 0$] and increasing the magnetic field at subsequent steps, usually with $\Delta H = 0.05 H_{c2}$. For each magnetic field we have calculated the magnetization taking averages after the thermodynamic equilibrium is established. In the simulations we have taken $T = 0.5$, $\eta = 12$ and we used a mesh of 120×120 points. In order to make efficient calculations we have chosen the time step (Δt) and the spatial discretization (Δx and Δy) depending on the value of κ . For example, for $\kappa = 0.15$ we used $\Delta x = \Delta y = 0.05$ and $\Delta t = 0.0025$; for $\kappa = 0.8$, $\Delta x = \Delta y = 0.3$ and

$\Delta t = 0.0025$ and for $\kappa = 2$, $\Delta x = \Delta y = 0.5$ and $\Delta t = 0.015$.

Figure 1(a) shows the case of a type I superconductor with $\kappa = 0.15$. We can see that the TDGL equations reproduce the basic phenomenology of type I superconduc-

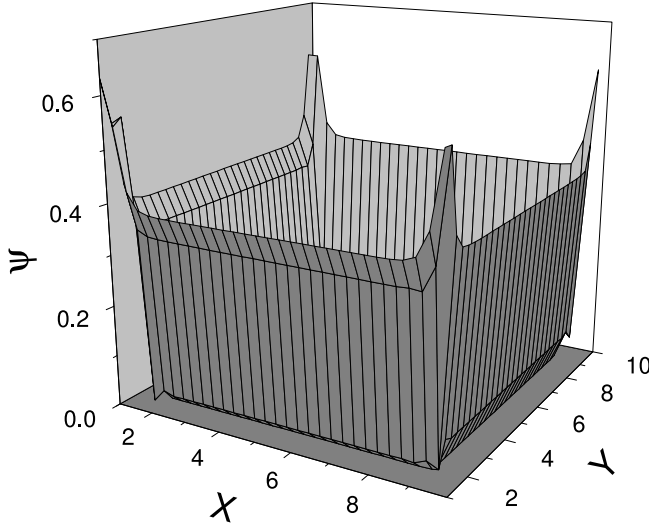


FIG. 3. Surface plot of the order parameter showing the state of surface superconductivity at $H = 0.55H_{c2}(0)$. The configuration of surface superconductivity shown in this figure was taken from the magnetization point of Figure 1(c) which is pointed out by an arrow.

tivity characterized by a sharp magnetic transition. In this case the superconductivity disappears abruptly and there is no surface superconductivity. The field profile is described by a Meissner state and $H = H_a \exp(-x/\lambda)$. Our simulations do not reproduce the known intermediate state structures of type I superconductors. This is because the dynamic equations considered here do not take into account the long range interaction between currents, i.e. demagnetization effects are neglected.

As it is known, the behavior of a type II superconductor is very different. Results for this case are shown in Figure 1(c). In this case the superconductor is in the Meissner state until a field H_p . At H_p some vortices enter the sample and a peak in the magnetization curve is generated. Above H_p the magnetization increases from negative values until the establishment of surface superconductivity for fields in the range $H_{c3} > H > H_{c2}$. The criterion for the appearance of surface superconductivity that we use is the disappearance of bulk superconductivity from the contour plots of the magnitude of the order parameter. The state of surface superconductivity is illustrated in Figure 3, which shows the spatial distribution of the order parameter for $H = 0.55H_{c2}$ just above $H_{c2}(T) = 0.5$. We can observe that in the corner

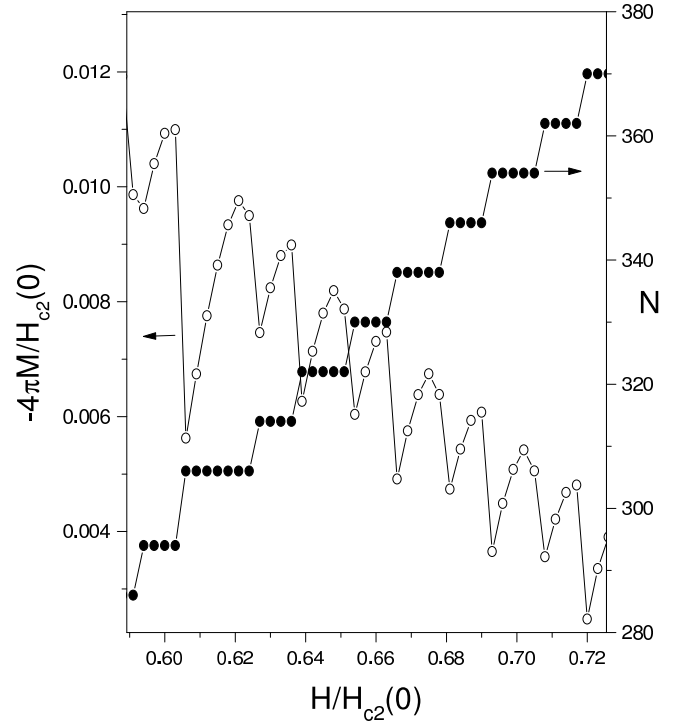


FIG. 4. Enhancement of the magnetization curve of Figure 1(c) in the region of surface superconductivity showing small magnetization peaks. In the right y axis we plot the number of vortices (N) that are inside the sample at different magnetic fields. The Figure emphasizes the correlation between the vortex entrance and magnetization behavior in the state of surface superconductivity.

of the sample the superconductivity is stronger than in the rest of the surface. In fact, when the surface superconductivity disappears there is also a field range where the superconductivity survives only at the corners.¹⁶ In the intermediate κ range ($\kappa = 0.8$), the Figure 1(b) shows that after the first magnetization peak there are other small peaks which appear because the surface superconductivity does not disappear gradually but at different steps. Each of these steps generates an small magnetization peak. A closer look to Figure 1(c) shows that this behavior is also present for $\kappa = 2$ but at a smaller scale. In fact, in Figure 4 it is shown an enhancement of the region of surface superconductivity of Figure 1(c) and also the magnetic behavior is correlated with the number of vortices inside the sample. The number of fluxoid quanta (N) in the computational domain can be calculated using the expression $N\Phi_o = \oint (A + \frac{J_s}{|\Psi|^2}) dl$ where Φ_o is the flux quantum. Figure 4 emphasizes that in the state of surface superconductivity the magnetic field still penetrates the sample in vortex avalanches, which generate the jumps in the magnetization observed in Figure 1(b). These vortex avalanches and magnetic jumps are

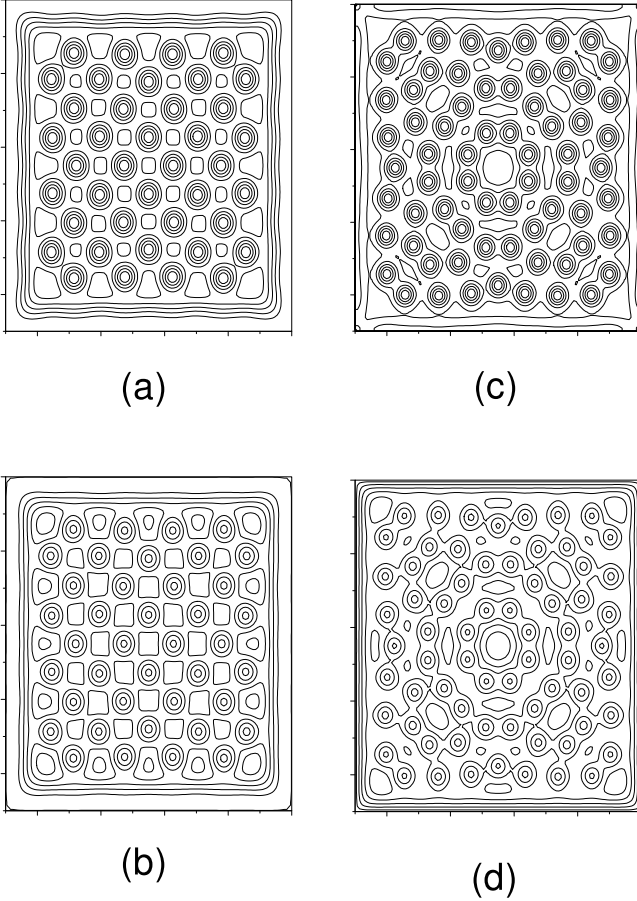


FIG. 5. Order parameter, (a) and (c), and magnetic field distributions, (b) and (d), of vortex states in equilibrium for different boundary conditions [S-N (a), (b) and S-I (c), (d)]. The applied magnetic field is $H = 0.25H_{c2}$ and $\kappa = 2$. Vortex locations are defined by local minima in Ψ and local maxima in B .

also present in Figure 1(c) but in a smaller scale.

The S-N boundary condition leads to a different magnetic behavior as can be observed in Figure 2 where we have used similar parameters as those reported in Figure 1. From the figure we can see that the dc magnetization curves reproduce the same phenomenology described above but without surface superconductivity, see Figures 2(b) and 2(c). Our numerical simulations show that for the S-N condition, the surface superconductivity is suppressed for all κ , in contrast with the S-I behavior. In the S-I case the magnetic field range where the surface superconductivity appears decreases with decreasing κ values, and the surface superconductivity finally disappears for $\kappa < 0.5$. These two results are in agreement with the analytical calculations of Ref. 18. For the S-I case they found surface superconductivity for $\kappa > 0.42$ and for $b \rightarrow 0$ (the S-N condition) the surface superconductivity was absent.

There are also differences in the order parameter and magnetic field distributions of vortices in the equilibrium states for different boundary conditions. The equilibrium

conditions for the S-I and the S-N interfaces at $H = 0.25H_{c2}(0)$ and $\kappa = 2$ are shown in Figure 5. In general,

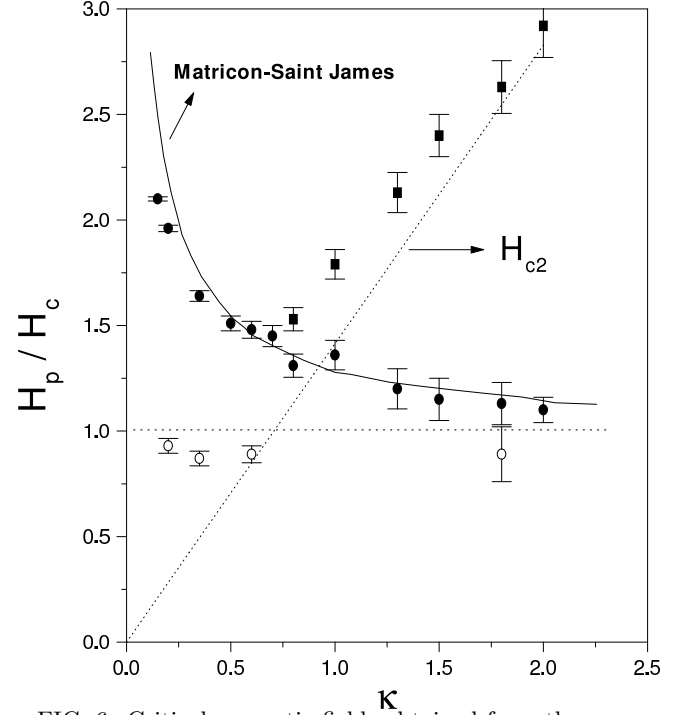


FIG. 6. Critical magnetic fields obtained from the magnetization curves at different κ values. For the S-I boundary condition are plotted the superheating field (H_p) (close circles) and the second critical field (H_{c2}) (closed squares). For the S-N boundary condition is plotted H_p (open circles). The dashed and dotted curves are the expected values of the thermodynamic critical field (H_c) and H_{c2} respectively. The continuous line is the result of H_p vs κ obtained by Matricon and Saint-James for a semi-infinite sample, observe the similitude with the result obtained in mesoscopic samples using the S-I boundary condition.

the vortex distribution in a finite-size superconductor depends fundamentally on the number of vortices and on the strength of the interaction between vortices and the surface currents. As it is shown in Figure 5, one of the main differences between the two boundary conditions is the number of vortices that for a fixed magnetic field are inside the sample. For the same samples size the S-N boundary condition always allows less vortices ($N = 40$ see Figures 5(a) and 5(b)) than the S-I condition ($N = 68$ see Figures 5(c) and 5(d)). Figure 5(a) also shows a more periodic distribution of vortices, almost a regular square lattice in contrast with the more irregular distribution of Figure 5(c). It is known that in the absence of interaction with the surface currents, as in an infinite superconductor, vortices arrange in a triangular vortex lattice because this configuration minimize the free energy. The energy of the square lattice of Figure 5 (a) is very close to the energy of the triangular lattice, then we can indirectly make the conclusion that for an S-N interface vortices

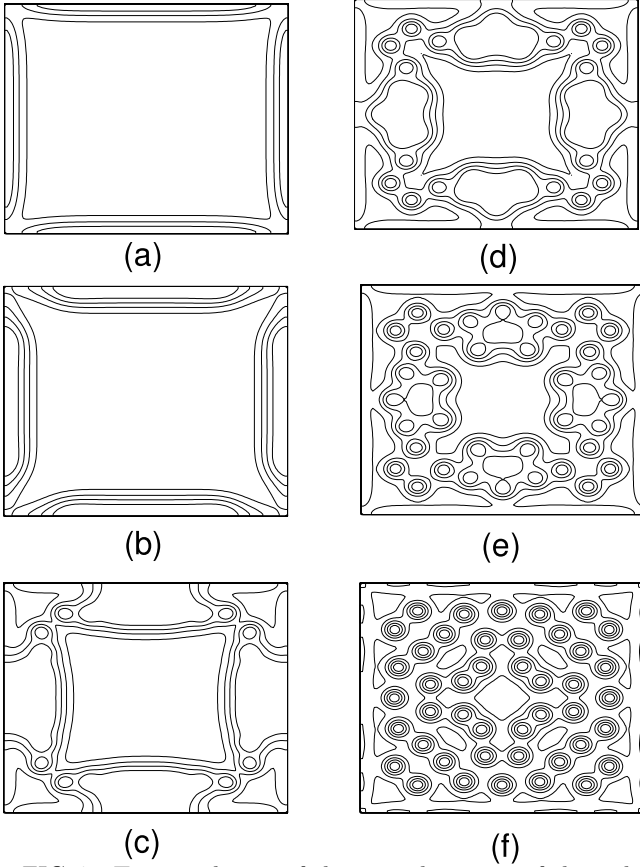


FIG. 7. Time evolution of the spatial pattern of the order parameter for the boundary condition $\Pi\Psi = 0$. The contour lines of $|\Psi|$ shown were taken with an interval 0.1 and the magnetic field is $H = 0.2H_{c2}(0)$, just above the first penetration field. The time interval between figures is $\Delta t = 250t_o$.

are less influenced by the surface currents than for an S-I interface. This is also related with the distance between the vortices and the sample surface. From Figure 5(a) we can see that the distance (h) between the vortices and the surface is $h_{SN} \approx 5\lambda$ a value larger than the value for a S-I interface $h_{SI} \approx 3\lambda$.

From the dc-magnetization curves we can obtain the first field for flux penetration H_p as a function of κ , this is shown in Figure 6. To our knowledge only Ref. 20 reports a calculation of H_p vs κ . This work addresses the problem of a semi-infinite medium making the assumption that the one-dimensional Ginzburg-Landau equation displays all the instabilities of interest. Very recently Vodolazov¹⁹ extended the previous result to analyze the effects of surface defects on $H_p(\kappa)$.

In the case of a semi-infinite medium without defects, the equations to be solved are:

$$\begin{aligned} \frac{d^2\Psi}{\kappa^2 dx^2} - A^2\Psi + \Psi - \Psi^3, \\ \frac{d^2 A}{dx^2} = \Psi^2 A \end{aligned} \quad (9)$$

with the boundary conditions:

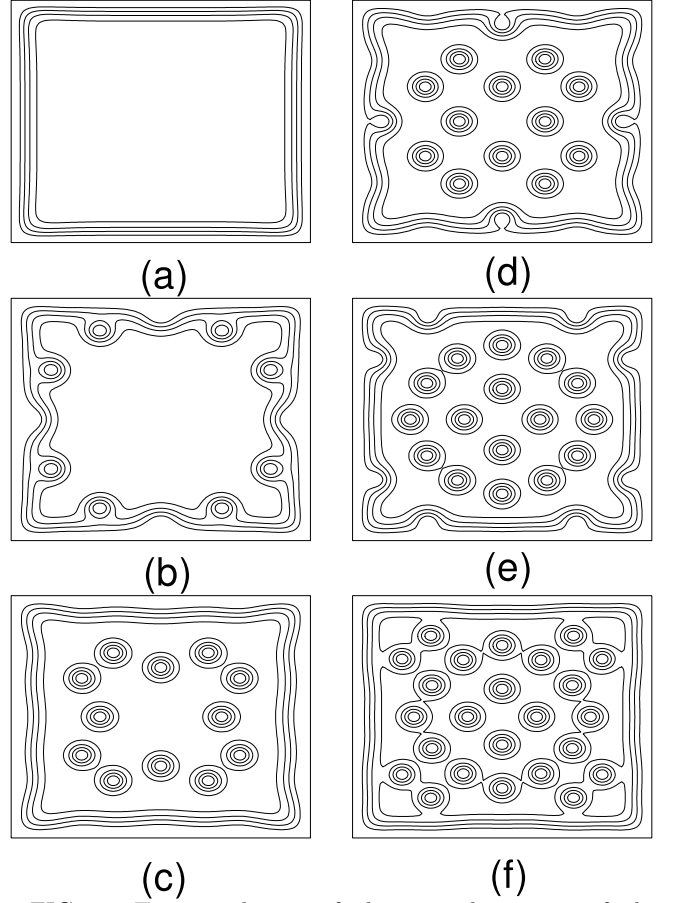


FIG. 8. Time evolution of the spatial pattern of the order parameter for the boundary condition $\Psi = 0$ at $H = 0.2H_{c2}(0)$ and $\Delta t = 250t_o$.

$$\begin{aligned} H = H_a \text{ and } \frac{d\Psi}{dx} = 0 \text{ at } x = 0 \\ A = H = 0 \text{ and } \Psi = 1 \text{ at } x = \infty \end{aligned} \quad (10)$$

Solving numerically equations (9) with the boundary condition (10) it is possible to find a relation among H_a and $\Psi(x=0) = \Psi_o$. Finally, the superheating field H_p is the maximum value of H_a that allows a physical meaning for Ψ_o , i.e. $0 < \Psi_o < 1$. The results obtained in this way are represented by the continuous-line of Figure 6. Our numerical results, on the other hand, are a numerical solution of the exact problem and are represented by closed circles. The H_p values reported here are the peaks of the simulated dc-magnetization curves and are normalized by H_c . Observe that H_p is always well above H_{c1} in the type II region ($H_{c1}(T) = [(\ln \kappa)/\sqrt{2}\kappa]H_c(T)$) and above H_c in the type I region, supporting the existence of the Bean-Livingston barrier. The error bars were calculated considering the error introduced by the discrete field step used in the calculation of the magnetization curves. Comparing our results with the continuous-line of Figure 6 we can conclude that, for an S-I interface, our numerical simulations show an increase of H_p with decreasing κ similar to the results obtained for the semi-

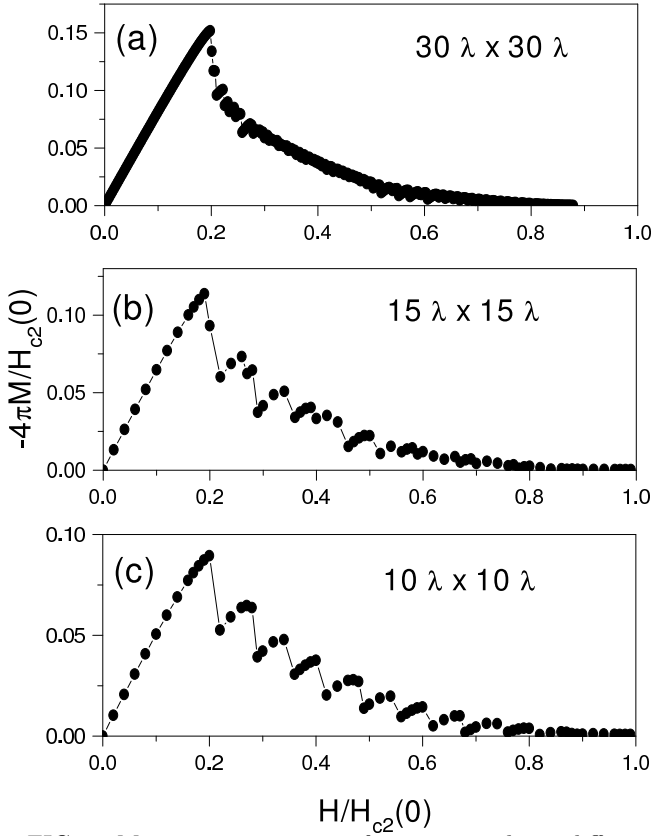


FIG. 9. Magnetization curves of square samples at different sizes and using the S-I boundary condition (a) $30\lambda \times 30\lambda$, (b) $15\lambda \times 15\lambda$ and (c) $10\lambda \times 10\lambda$.

infinite medium. For $\kappa = 0.15$ this result persists even for samples as small as $6\xi \times 6\xi$ ($40\lambda \times 40\lambda$) [see Figure 1(a)]. For $\kappa \rightarrow \infty$ we obtain that $H_p \rightarrow H_c$, in agreement with a result first obtained by de Gennes.¹⁷

Figure 6 also shows that in the type II region the H_{c2} values obtained from the S-I simulations (closed squares) are near to the expected values ($H_{c2}(T) = \sqrt{2}\kappa H_c(T)$ dotted line), but some differences appear at small κ , especially near the type I region. This may be understood by noting that in the intermediate κ region the field H_p is close to H_{c2} , and a delay of the superconducting-normal transition could be expected.

The behavior of H_p vs κ is very different when the S-N boundary condition is used. In this case, H_p is independent of κ and nearly equal to H_c (see the open circles of Figure 6). This result implies that in the case of the S-N interface of a type II superconductor there exist a barrier for flux penetration that is slightly lower but approximately equal to the barrier that appears in the S-I interface. In this case, the main effect of the S-N boundary is to forbid the possibility of surface superconductivity and thus there is not an H_{c3} critical field. On the other hand, in the type I region the S-N boundary condition completely suppresses the Bean-Livingston barrier and the flux penetration takes place at H_c .

The use of the TDGL equations also allows to study the dynamics of vortex penetration for different boundary

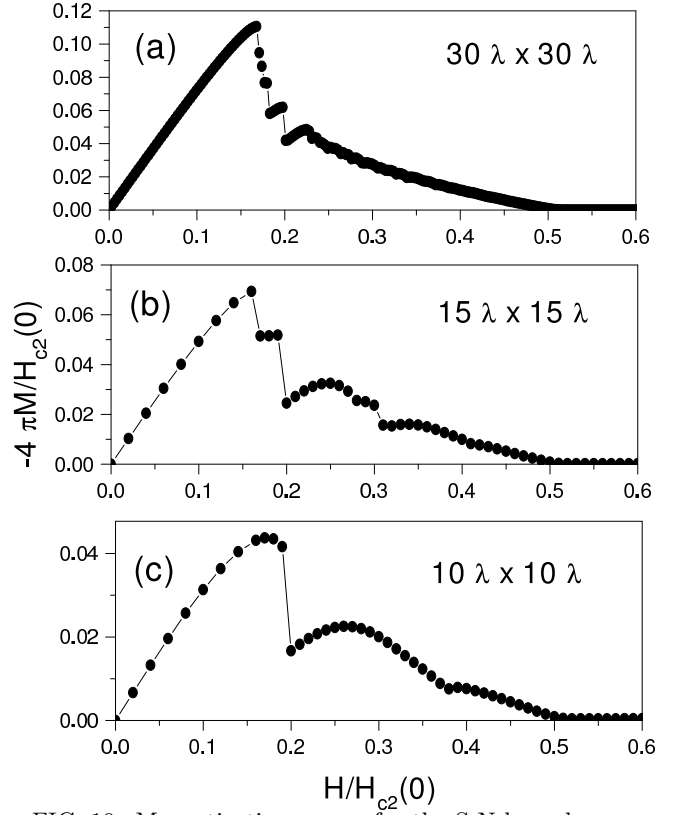


FIG. 10. Magnetization curves for the S-N boundary condition. We show the magnetic curves at different sample sizes from the macroscopic to the mesoscopic-like behavior: (a) $30\lambda \times 30\lambda$, (b) $15\lambda \times 15\lambda$ and (c) $10\lambda \times 10\lambda$.

conditions. It is particularly important to study the way that the first vortex penetration takes place just at $H = H_p$. Figures 7 and 8 show the dynamic evolution of the order parameter when the field is increased above H_p from a previous Meissner state until the thermodynamic equilibrium is again established. If the interface is of the S-I type, vortices enter the sample at the same time in a unique avalanche, as a collective phenomenon (see Figure 7). In these case, the order parameter at the sample interface is different from zero in the Meissner state. When the condition for vortex entrance is fulfilled the order parameter at each boundary point starts to decrease until reaching zero, and there is an intermediate time interval when $\Psi = 0$ at the boundary. Just in this moment all the vortices enter the sample (see Figs.7(c-e)) and afterwards the order parameter at the boundary increases again to a non-zero value. It is interesting to note that this process is always necessary for vortex penetration in S-I interfaces, there is always an intermediate $\Psi = 0$ state at the boundary. Finally Figure 7(d) shows the vortex distribution at equilibrium.

On the contrary, a gradual entrance of vortices is observed for an S-N interface (see Figure 8). For this boundary condition the order parameter at the interface is zero and the intermediate condition is always fulfilled. In this case the vortex entrance is an individual phenomenon

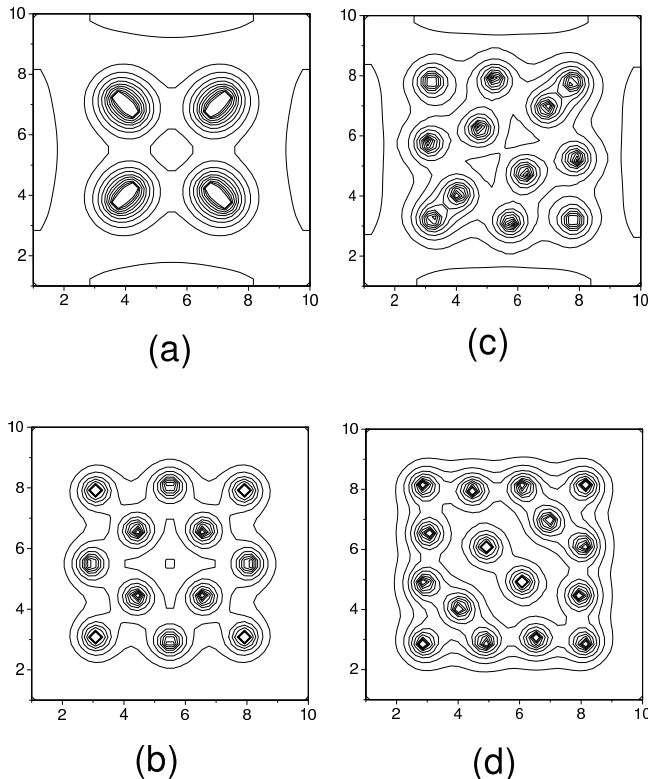


FIG. 11. Spatial distribution of the order parameter in the vicinity of vortex penetrations using the S-I boundary condition in a $10\lambda \times 10\lambda$ sample. We show distributions after two-vortex and four-vortex penetrations (a) $N = 8, H = 0.34H_{c2}(0)$; (b) $N = 12, H = 0.36H_{c2}(0)$; (c) $N = 12, H = 0.4H_{c2}(0)$ and (d) $N = 16, H = 0.42H_{c2}(0)$.

and the number of vortices inside the sample increases gradually. The equilibrium condition is established when the vortices inside the sample repel the entrance of new vortices. A mixed dynamical behavior would appear in an S-I interface with defects. At the defects the order parameter is depressed and therefore $\Psi = 0$ is already established at some boundary points, which are preferred points for vortex entrance. In this sense, the S-N boundary condition will also reproduce the behavior of a superconductor with a high density of defects at the boundary.

IV. FINITE-SIZE EFFECTS IN MESOSCOPIC TYPE II SUPERCONDUCTORS

The magnetic behavior of mesoscopic superconductors is different from the behavior of bulk samples. In a mesoscopic scale, several maxima appear in the magnetization curves which are related to the vortex entrance. This result is quite general and appears either in thin films²¹ or mesoscopic superconducting disks.^{7,11} In this section we study the magnetic behavior of superconducting samples of different sizes, in particular we cover the sample size region where a transition from a mesoscopic to a bulk behavior takes place. We show that in the mesoscopic

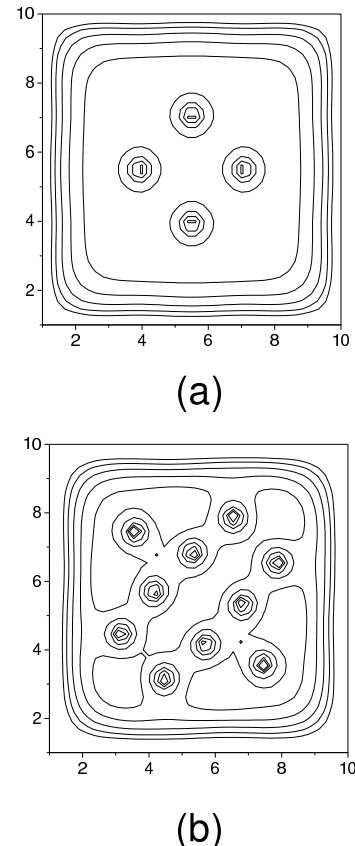


FIG. 12. Spatial distribution of the order parameter in the vicinity of vortex penetrations using the S-N boundary condition in a $10\lambda \times 10\lambda$ sample. (a) $N = 4, H = 0.27H_{c2}(0)$; and (b) $N = 10, H = 0.41H_{c2}(0)$.

scale there is also a different magnetic behavior depending on the boundary condition.

Figure 9 shows the dc-magnetic behavior of superconducting square samples of different sizes with S-I boundary condition. The behavior of Fig.9(a) is typical of the macroscopic samples that we have study in the previous section, however if we decrease the sample size to the mesoscopic region the continuous behavior disappears and some magnetization maxima appears (see Figs.9(b) and (c)). The discontinuities in the magnetization are related to the penetration of vortices into the sample. It is interesting to note that the magnetization maxima appear even in the region of surface superconductivity, emphasizing that also in the state of surface superconductivity the magnetic field penetrates in quantized units (see also Figure 4).

When we use the S-N boundary condition there are some similarities with the S-I magnetic behavior. In the S-N case we also observe that there are macroscopic and mesoscopic regimes and a transition region between them. We also obtain similar H_p values in both cases. But, as it is shown in Figure 10(c) the mesoscopic behavior is now different: there is an appreciable decrease in the number of magnetization maxima and the transition between the states of the system with a different

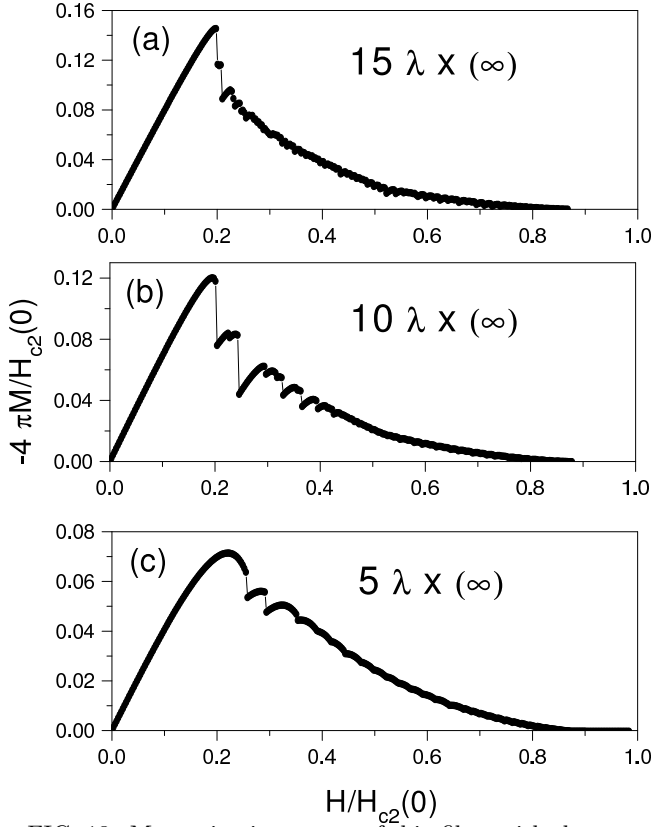


FIG. 13. Magnetization curves of thin films with the external magnetic field applied parallel to the film. The curves are generated for decreasing thicknesses of the film and using the S-I boundary condition. (a) $15\lambda \times \infty$, (b) $10\lambda \times \infty$ and (c) $5\lambda \times \infty$.

number of vortices is more continuous. The decrease in the number of entrance events for the S-N boundary in mesoscopic samples is related to the fact that this boundary condition allows a higher field penetration in the Meissner state. At the same magnetic field the mean magnetization values of the Meissner state are lower in the S-N case than in the S-I case as can be observed comparing Figures 9(c) and 10(c). Then, a small sample with an S-N boundary only needs a few penetration events to arrive to the normal state. As we analyzed before, the vortex penetration for the S-N boundary occurs gradually, as an individual phenomenon, which allows a more continuous transition between the different vortex states and a more continuous magnetization curve.

Figure 11 and Figure 12 show changes in the vortex distribution just in the vicinity of a magnetization discontinuity, i.e. when a vortex penetration takes place. In the case of the S-I boundary Figure 11(a) shows the vortex distribution at $H = 0.34H_{c2}(0)$ when there are 8 vortices inside the sample. When we increase the magnetic field to $H = 0.36H_{c2}(0)$ 4 new vortices penetrate the sample and there is a rearrangement of vortex positions as it is shown in Figure 11(b). Figure 11(c) shows the vortex distribution just before the next vortex entrance that takes place at $H = 0.42H_{c2}(0)$. The increase

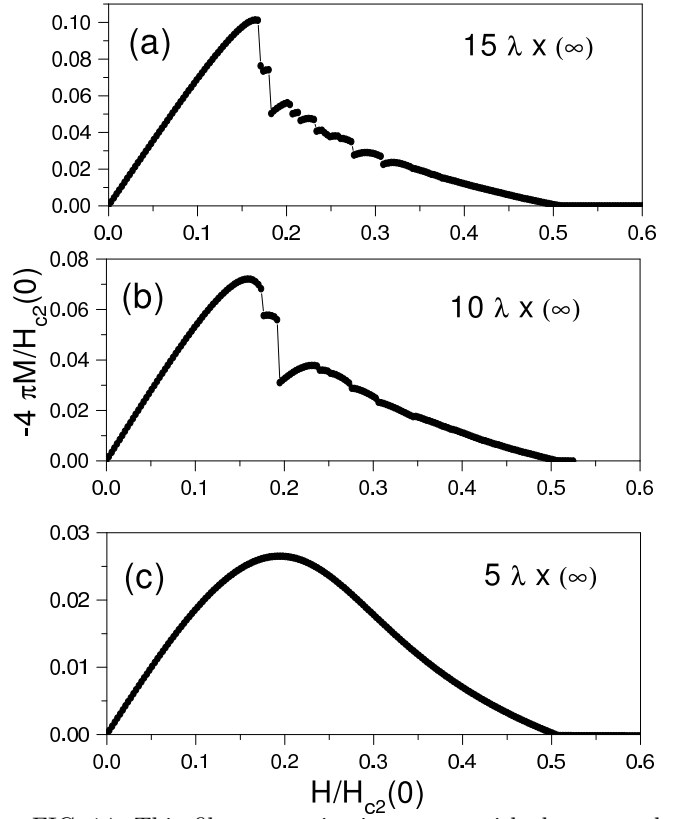


FIG. 14. Thin film magnetization curves with the external field applied in the same geometry of Figure 13 but using the S-N condition: (a) $15\lambda \times \infty$, (b) $10\lambda \times \infty$ and (c) $5\lambda \times \infty$. As it is observed for samples sizes as low as $5\lambda \times \infty$, Figure 14 (c), there is a continuous transition to the normal state.

in the external magnetic field from $H = 0.36H_{c2}(0)$ to $H = 0.40H_{c2}(0)$ changes the distribution of the 12 vortices as can be observed in Figure 11(b) and Figure 11(c). Finally, after the 4 new vortices penetrate the sample, there is a new vortex rearrangement as it is shown in Figure 11(d). From Figure 11 it is possible to observe that all the vortex configurations are symmetric respect to the diagonals of the square but besides this symmetry restriction the vortex distribution seems to be arbitrary, there is a great richness of possible configurations. The equilibrium vortex configurations in the vicinity of vortex penetrations events calculated using the S-N boundary condition are shown in Figure 12. The behavior is very similar to the behavior shown by the S-I boundary, but in general vortices are less confined at the same magnetic field.

The transition from the macroscopic to the mesoscopic behavior is quite general and does not depends on the sample geometry. We also study the magnetic behavior of a thin film with the field parallel to its faces. In this case there is only one relevant dimension, the thickness of the film (d). We work here with the case $d > \lambda$. Figure 13 shows the magnetic behavior of thin films with different thickness obtained using the S-I boundary condition. We can observe that in this case the discontinuities in the

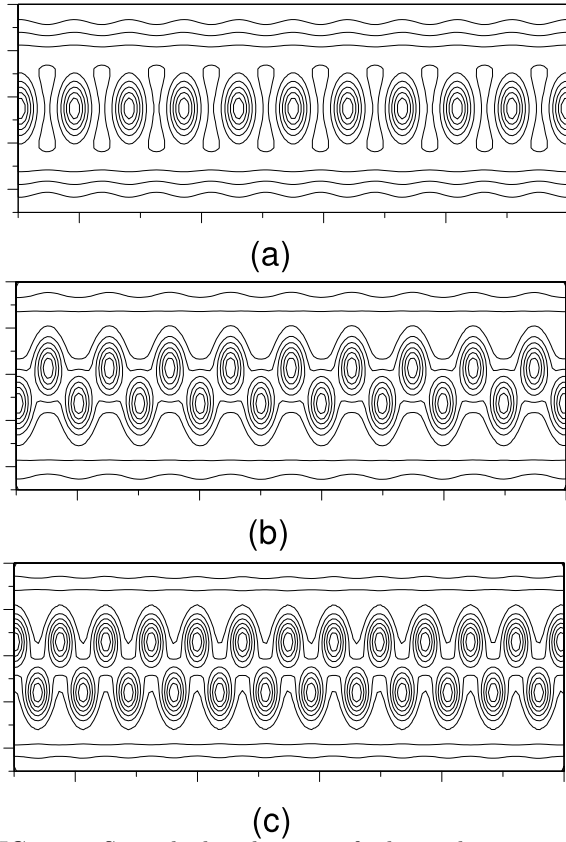


FIG. 15. Spatial distribution of the order parameter around two magnetization jumps in a thin film of size $7.5\lambda \times \infty$. We use the S-I boundary condition. Figures are generated increasing the magnetic field: (a) $N = 10, H = 0.252H_{c2}(0)$; (b) $N = 18, H = 0.255H_{c2}(0)$ and (c) $N = 24, H = 0.297H_{c2}(0)$.

magnetization curves appear at smaller film thickness but they are less important than in squares samples, possibly because vortices in a mesoscopic square sample are more confined than in thin films of the same dimension. We have also done numerical calculations of the magnetic behavior in thin films using the S-N boundary condition (see Figure 14). In particular Figure 14(c) shows that for very small film thickness the first order phase transition changes to a continuous transition. When the transition is continuous, vortex lines do not penetrate the sample and the superconducting state disappears gradually. This behavior is also present when we use the S-I boundary condition but it is necessary to explore lower sample sizes than the one shown in the corresponding figures.

Some vortex configurations observed in thin films using the S-I and S-N boundary conditions are shown in Figures 15 and 16 respectively. In both cases the vortex configurations are symmetric to a plane parallel to the thin film faces.

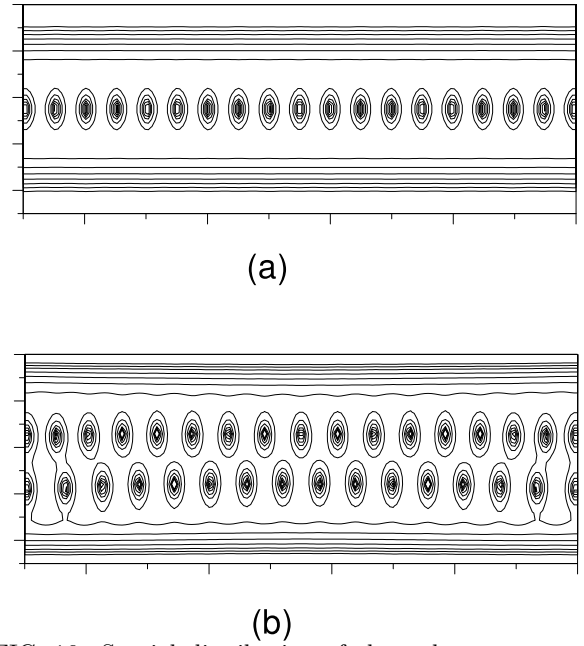


FIG. 16. Spatial distribution of the order parameter for magnetic fields in the vicinity of a vortex entrance. We use a thin film of size $7.5\lambda \times \infty$ with the S-N boundary condition. (a) $N = 18, H = 0.351H_{c2}(0)$; and (b) $N = 31, H = 0.357H_{c2}(0)$.

V. MULTIPLE PENETRATION FIELDS IN MESOSCOPIC SAMPLES

What causes the transition from a macroscopic to a mesoscopic behavior? To answer this question we will make an energy analysis. It is known that the Gibbs free energy (G) of a vortex line located a distance x from the sample surface can be calculated using the expression:¹⁷

$$G = \frac{\Phi_o}{4\pi} [H_a \exp(-\frac{x}{\lambda}) - \frac{1}{2} \frac{\Phi_o}{2\pi\lambda^2} K_o(\frac{2x}{\lambda}) + H_{c1} - H_a] \quad (11)$$

where H_a is the external magnetic field and K_o is the modified Bessel function of the second kind. In normalized units the above expression reads:

$$\frac{4\pi G}{H_{c2}\Phi_o} = [H_a \exp(-\frac{x}{\lambda}) - \frac{1}{2k^2} K_o(\frac{2x}{\lambda}) + \frac{\ln \kappa}{2\kappa^2} - H_a] \quad (12)$$

where we have used the relation $H_{c1} = (\ln \kappa)/2\kappa^2 H_{c2}$. The first term of Equations (11) and (12) is related with the repulsive interaction between the vortex line and the external field, the second term describes the attraction between the vortex and the surface currents, this term is usually represented through the interaction with an image vortex⁴ and the third term is the vortex self energy.

The above expressions are valid when there are no vortex lines inside the sample. If there are vortex lines located inside the sample, some additional terms due to

the interaction between vortex lines are needed. In the following we will suppose that there is only one vortex inside the sample located at position l and that we are analysing the Gibbs free energy in the same line perpendicular to the sample surface. If l is small, the new vortex that is trying to enter the sample now feels two additional terms both representing attractive interaction to the surface. The first term is the repulsive force between the vortex lines and the second is the attractive interaction with the image of the vortex located inside the sample. The last term is needed in order to take into account the perturbation of the vortex already inside the sample because of its proximity to the surface. Both contributions are more important in mesoscopic superconductors as we will show below. The free energy that gives the correct force expression is:

$$\frac{4\pi G}{H_{c2}\Phi_0} = H_a \exp\left(-\frac{x}{\lambda}\right) - \frac{1}{2\kappa^2} K_o\left(\frac{2x}{\lambda}\right) + \frac{\ln \kappa}{4\kappa^2} - H_a + \frac{1}{\kappa^2} K_o\left(\frac{l-x}{\lambda}\right) - \frac{1}{\kappa^2} K_o\left(\frac{l+x}{\lambda}\right) \quad (13)$$

Equations (12) and (13) are approximate expressions and have the limitation that they are not valid near the sample surface, then we will only use it for $x > \xi$. However, is useful to note that in a more exact treatment we would obtain that $G \rightarrow 0$ when $x \rightarrow 0$ because the Gibbs free energy of a vortex located outside the sample must be zero.

Figures 17(a), 17(b) and 17(c) were generated using Equation (12) for $\kappa = 2$. The free energy of the vortex depends on both the applied magnetic field and the distance to the surface. For $H < H_{c1}$ the free energy associated with a vortex is positive at all x values, as it is shown in Figure 17(a), vortices are then thermodynamically unstable inside the superconductor and there is an energy cost associated with the vortex entrance. The thermodynamic condition for vortex penetration is not fulfilled until $H > H_{c1}$, when the free energy of a vortex located well inside the superconductor becomes negative, see Figure 17(b). However, Figure 17(b) also shows that because of the attractive interaction between the vortex and the surface currents a barrier to vortex entrance appears nears the surface. This is the Bean-Livingston barrier that we analyzed in the previous section. Taking into account Equation (12) it is possible to estimate H_p as the magnetic field for which the expression $(\partial G/\partial x)_{x=\xi}$ becomes negative, i.e. when the maximum of $G(x)$ moves inside the region $x < \xi$. This condition is approximately fulfilled at $H = 0.24H_{c2}$ as it is shown in Figure 17(c). At $H = H_p$ some vortices penetrate the sample and the free energy associated with the entrance of a new vortex now must be calculated using an analogous to Equation (13), the exact expression depends of the number of vortices and its location inside the sample. Considering only one vortex located at $x = 3\lambda$ and using Equation (13) we have calculated the free energy just after the first vortex entrance ($H = 0.24H_{c2}$), the results are shown in Figure

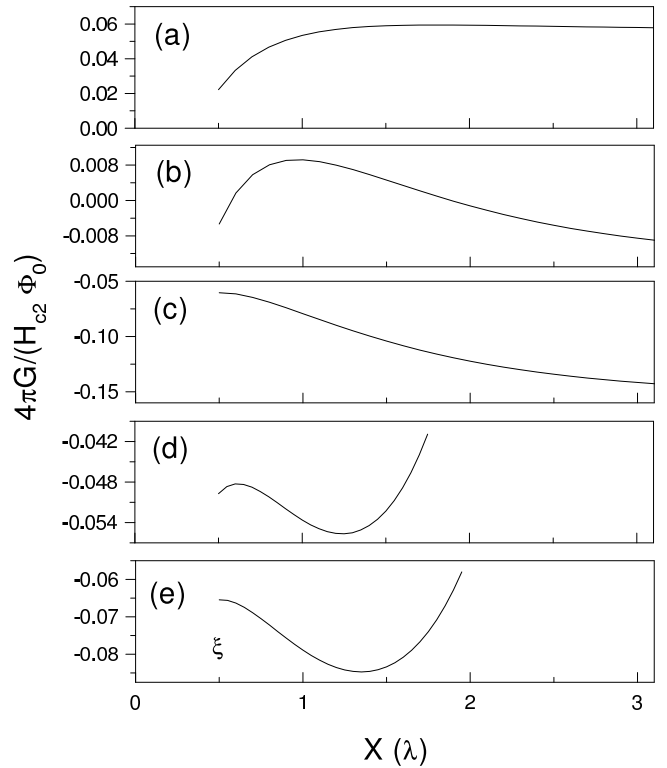


FIG. 17. Gibbs free energy of a vortex line as a function of the distance $x(\lambda)$ from the sample surface. We have used Equation (12) for (a) $H = 0.03H_{c2}$, (b) $H = 0.1H_{c2}$, (c) $H = 0.24H_{c2}$ and Equation (13) for (d) $H = 0.24H_{c2}$ and (e) $H = 0.28H_{c2}$.

17(d). Observe that the free energy changes considerably from Figure 17(c) to figure 17(d). Now there are three relevant regions: i) near $x = 3\lambda$, there is a region where the Gibbs free energy increases with increasing x , the strong repulsive interaction with the vortex inside the sample dominates; ii) there is an intermediate region where G decreases at increasing x , this means that a vortex located in this region will be pulled inside the sample, it is possible to allocate vortices in this region and there is also a region iii) near the sample surface that repels vortex entrance, G increases for increasing x . The existence of regions ii) and iii) means a reinforcement of the surface barrier induced by vortex penetration and allows magnetic field intervals of metastable states. This energy barrier reinforcement due to vortex entrance is more important in mesoscopic superconductor because, in small samples, vortices are confined by the potential well generated by the sample surface and must stay fixed in a position close to the surface. For example in an $10\lambda \times 10\lambda$ square sample, vortices are constrained to be located around the center of the sample at $x = 5\lambda$, because of its interaction with the surface currents. As a consequence vortices stay at their position $x \approx 5\lambda$ generating a new surface barrier and it is necessary a considerable magnetic field increase to allow new vortex penetration, there is a magnetic field interval where the system is in a metastable state. For macroscopic samples the situation

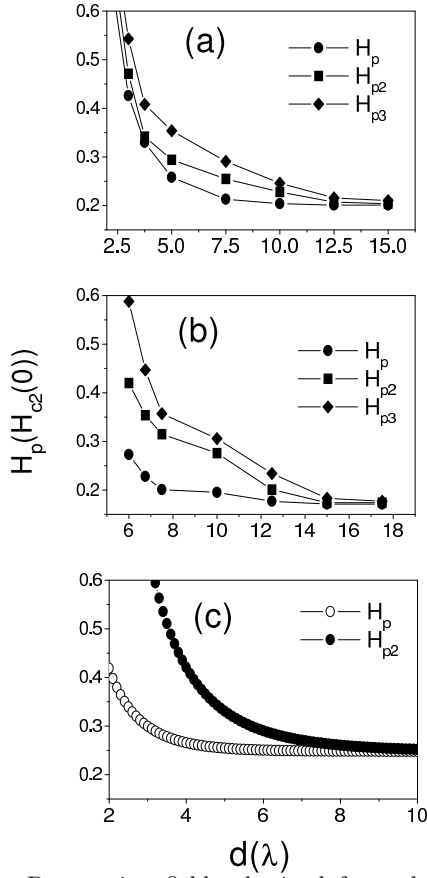


FIG. 18. Penetration fields obtained from the magnetic curves shown in Figures 13 and 14. We plot the first, second and third penetration fields at different film thickness for (a) S-I and (b) the S-N boundary condition. $H_{p3} \neq H_{p2} \neq H_p$ is typical of a mesoscopic behavior. For large film thickness, in the region of the macroscopic behavior, a continuous entrance of vortices is recovered ($H_{p3} \rightarrow H_{p2} \rightarrow H_p$). Figure (c) shows an estimation of H_p and H_{p2} using the image method and considering the influence of the sample size in the field profile.

is quite different, there is a more continuous vortex penetration. In macroscopic samples the vortices that are inside the sample are not confined and they do not have serious restriction in its movement because they can be allocated very far from the surface and they can move freely inside the sample. In this case, a small increase of the magnetic field is enough to accommodate new vortex lines, as can be observed in Figure 9(a).

From the analysis of Figures 9, 10, 13, 14 and the previous discussion we can conclude that in mesoscopic samples for both boundary conditions, there are preferred values of magnetic field for vortex penetration, in this case the process of vortex entrance is discontinuous in contrast with the continuous macroscopic regime. This behavior is a consequence of the barrier to vortex entrance that appears after each penetration event. In this way we can define a second penetration field H_{p2} , a third penetration field H_{p3} and so on. We observe that after increasing the size of the sample the vortex penetration

becomes continuous ($H_{p3} \rightarrow H_{p2} \rightarrow H_p$).

The exact delimitation of the macroscopic and mesoscopic regimes depends on the geometry of the sample. We will study in detail here the behavior of a thin film because is a simpler case with only one significant dimension. The size dependence of the penetration fields obtained in a thin film using the S-I boundary condition are summarized in Figure 18(a). For $d > 15\lambda$ a continuous vortex penetration is observed, this is the region of a macroscopic behavior, the mesoscopic region is located at $2\lambda \lesssim d \lesssim 15\lambda$. For $d < 2\lambda$ the second order phase transition transforms into a continuous transition. Figure 18(b) shows the sample size dependence of the first, second and third penetration field of thin films using an S-N boundary condition. For the S-N boundary the macroscopic behavior appears at $d > 18\lambda$, the mesoscopic regions is located between $5\lambda \lesssim d \lesssim 18\lambda$ and for a $d < 5\lambda$ the continuous transition appears.

It is interesting to note that H_p is size dependent only in the mesoscopic region. This behavior can be explained studying the size dependence of the different terms in Equation (12). The term generated by the magnetic field $H \exp(-x/\lambda)$ now becomes $H \cosh[(x-d)/\lambda] / \cosh(d/\lambda)$ due to the proximity of the other surface, the magnetic force that pulls the vortex inside the sample decrease when the film thickness (d) decreases. The image term also changes because the vortex lines that are trying to enter the sample are now near both surfaces and new image lines are necessary in order to satisfy the boundary condition at both surfaces. The application of the image method to parallel surfaces gives an infinite number of images, but the net effect is the apparition of an attractive interaction to the new surface. Then, in the mesoscopic region, there is also a decrease in the net attractive image force. If we consider only three relevant terms in the image forces, the normalized force $f = (4\pi/\Phi_0 H_{c2})\lambda(\delta G/\delta x)$ that feels a vortex line that is trying to enter when the sample is in the Meissner state can be estimated by:

$$f = H_a \frac{\sinh(\frac{x-d/2}{\lambda})}{\cosh(d/2\lambda)} + \frac{1}{\kappa^2} K_1\left(\frac{2x}{\lambda}\right) - \frac{1}{\kappa^2} K_1\left(\frac{2d-2x}{\lambda}\right) + \frac{1}{\kappa^2} K_1\left(\frac{2d+2x}{\lambda}\right) \quad (14)$$

where d is the thickness of the film and we have chosen f positive when it repels the vortex entrance. As we analyzed before, H_p is usually defined as the magnetic field that makes $f|_{x=\xi} = 0$. This condition leads to the following expression for H_p :

$$H_p = \frac{[K_1(\frac{2\xi}{\lambda}) - K_1(\frac{2d-2\xi}{\lambda}) + K_1(\frac{2d+2\xi}{\lambda})] \cosh(\frac{d}{2\lambda})}{\kappa^2 \sinh(\frac{d-2\xi}{2\lambda})} \quad (15)$$

We have evaluated this behavior of $H_p(d)$ in Figure 18(c). As can be observed, when we decrease the thickness of the film the repulsive magnetic force decreases

more quickly than the attractive term, and the H_p values increases. This was previously shown in the numerical simulations of Figure 18(a) and 18(b).

In Figure 18(c) we also estimate the behavior of the second penetration field H_{p2} as a function of the sample size. The approximate expression used was obtained including in the Equation (15) the extra terms related with the presence of a vortex line inside the sample as we did in Equation (13). For simplicity we have considered one vortex located at the middle of the sample at $x = d/2$. Under this condition H_{p2} becomes:

$$H_{p2} = [K_1(\frac{2\xi}{\lambda}) - K_1(\frac{2d-2\xi}{\lambda}) + K_1(\frac{2d+2\xi}{\lambda}) + K_1(\frac{d-2\xi}{2\lambda}) + K_1(\frac{d+2\xi}{2\lambda}) - K_1(\frac{3d+2\xi}{2\lambda})] \frac{\cosh(\frac{d}{2\lambda})}{\kappa^2 \sinh(\frac{d-2\xi}{2\lambda})} \quad (16)$$

this expression also reproduces the H_{p2} sample size dependence observed in the numerical simulations. This simple model reproduces qualitatively the mesoscopic as well as the macroscopic behavior obtained in the numerical simulations at similar values of the film thickness.

VI. SUMMARY

We have presented results on the study of the demagnetization curves and the Bean-Livingston barrier for type I and type II superconductor using different boundary conditions. Our results show that there is an appreciable change in the strength of the Bean-Livingston barrier depending on the boundary. We observe that the dynamics of the vortex penetration depends on the type of the surface boundary. If the interface is of the S-I type, vortices enter the sample at the same time in a unique avalanche, as a collective phenomenon, but for the S-N boundary condition the vortex entrance is an individual phenomenon: the number of vortices increases gradually.

We also studied the reinforcement of the surface barrier due to the presence of vortex lines inside mesoscopic superconductors. We show that these new barriers allow the existence of metastable states that are very important in the magnetic behavior of the mesoscopic samples. In this way, we study magnetization curves at different sample dimensions in the region where the transition from a macroscopic to a mesoscopic behavior takes place and we obtain the sample size dependence of the first, second and third penetration fields for the S-I and S-N boundary conditions. We finally show that for sufficiently large sample sizes the continuous macroscopic regimen is recovered, i.e. $H_{p3} \rightarrow H_{p2} \rightarrow H_p$.

ACKNOWLEDGMENTS

We acknowledge helpful discussions with Arturo López and Niels Grønbech-Jensen. One of us (A.D.H.) also acknowledges Oscar Arés for useful comments and help. A.D.H. also acknowledges the Centro Latino-Americano de Física (CLAF) for financial support and D.D. acknowledges support from Conicet and CNEA (Argentina). We also acknowledge the financial support for this project from ANPCyT and Fundación Antorchas.

-
- ¹ A. K. Geim et. al., Nature **396**, 144 (1998).
 - ² C. A. Bolle, V. Aksyuk, F. Pardo, P. L. Gammel, E. Zeldov, E. Bucher, R. Boie, D. J. Bishop and D.R. Nelson, Nature **399**, 43 (1999).
 - ³ A. K. Geim, S. V. Dubonos, I. V. Grigorieva, F. M. Peeters and V. A. Shweigert, Nature **407**, 55 (2000).
 - ⁴ C. P. Bean and J. D. Livingston, Phys. Rev. Lett. **12**, 14 (1964).
 - ⁵ Y. Enomoto and K. Okada, J. Phys. Cond. Matter **9**, 10203 (1997).
 - ⁶ E. B. Sonin and K. B. Traito, Phys. Rev. B, **50**, 13547 (1994).
 - ⁷ P. Singha Deo, V. A. Shweigert, F. M. Peeters and A. K. Geim, Phys. Rev. Lett. **79**, 4653 (1997).
 - ⁸ V. A. Shweigert, F. M. Peeters and P. Singha Deo, Phys. Rev. Lett. **81**, 2783 (1998).
 - ⁹ V. A. Shweigert and F. M. Peeters, Phys. Rev. B **57**, 13817 (1998).
 - ¹⁰ V. A. Shweigert and F. M. Peeters, Phys. Rev. Lett. **83**, 2409 (1999).
 - ¹¹ V. A. Shweigert and F. M. Peeters, Phys. Rev. B **60**, 3084 (1999).
 - ¹² A. V. Kuznetsov, D. V. Eremenko, V. N. Trofimov, Phys. Rev. B **59**, 1507 (1999).
 - ¹³ P. Singha Deo, V. A. Shweigert and F. M. Peeters, Phys. Rev. B **59**, 6039 (1999).
 - ¹⁴ L. P. Gorkov and G. M. Eliashberg, Soviet Phys.-JETP **27**, 328 (1968).
 - ¹⁵ W. D. Groop, H. G. Kaper, G. L. Leaf, D. M. Levine, M. Palumbo and V. M. Vinokur, J. Comp. Phys. **123**, 254 (1996).
 - ¹⁶ R. Kato, Y. Enomoto and S. Maekawa, Phys. Rev. B **47**, 8016 (1993).
 - ¹⁷ P. G. de Gennes: Superconductivity of metals and alloys (Adison-Wesley) 1989.
 - ¹⁸ J. O. Indekeu and J. M. J. van Leeuwen, Phys. Rev. Lett. **75**, 1618 (1995).
 - ¹⁹ D. Vodolazov, Phys. Rev. B **62**, 8691 (2000).
 - ²⁰ J. Matricon and D. Saint-James, Phys. Lett. **24A**, 241 (1967).
 - ²¹ C. Bolech, G. C. Buscaglia and A. López, Phys. Rev. B, **52**, R15719 (1995).